Indian Journal of Engineering & Materials Sciences
Vol. 33, June 2026, pp. 377-389
DOI: 10.56042/ijems.v33i03.27549

Engineered graphene oxide functionalization strategy over $MnFe_2O_4$ magnetic nanoparticles toward magnetic inductive heating

Rojaleena Das[a*], Himani Bhardwaj[b], Pratibha Sharma[c], Mandar Joshi[d], Archana Sahoo[e], Deepika Gupta[c] & Nitish Kaushik[g]

[a]Department of Mechanical Engineering, Lingaya's Vidyapeeth, Faridabad 121 002, Haryana, India
[b]Department of Electronics & Communication Engineering, Lingaya's Vidyapeeth, Faridabad 121 002, Haryana, India
[c]School of Basic Science, Lingaya's Vidyapeeth, Faridabad 121 002, Haryana, India
[d]Department of Metallurgy, Dr S & SS Ghandhy College of Engineering & Technology, Surat 395 001, Gujarat, India
[e]Department of Physics, Rao Pahlad Singh Degree College, Balana, Mahendragarh, Haryana, 123 029, India
[f]School of Automation, Banasthali Vidyapith, Rajasthan 304 022, India

Received:14 January 2026 ; Accepted:17 May 2026

Magnetic inductive heating of magnetic nanoparticles (MNPs) represents a promising non-invasive therapeutic approach for cancer treatment. In the present study, oxygen-rich graphene oxide has been surface functionalized over superparamagnetic $MnFe_2O_4$ (GO@MF1) MNPs prepared through a best-suited sonication-assisted hydrothermal method. The X-ray diffraction has confirmed the formation of phase-pure cubic spinel $MnFe_2O_4$ nanoparticles and graphene oxide with an interlayer spacing of 8.21 Å. The GO@MF1 MNPs have exhibited high aqueous colloidal stability with enhanced zeta potential of −40 mV. The static magnetic measurement has confirmed excellent superparamagnetic behavior of GO@MF1 with a saturation magnetization of 56 emu/g and minimized coercivity of 17 Oe. The strong surface functionalization in $MnFe_2O_4$ has increased thermal stability of GO@MF1 up to 400°C, and minimized the agglomeration through strong electrostatic repulsion through oxidized graphene. The 2 mg/mL aqueous colloidal solution of GO@MF1 has been utilized for inductive heating experiments at an alternating magnetic field of 12 mT at 585.6 kHz frequency. The choice of magnetic field and frequency has demonstrated remarkable hyperthermia performance, with the GO@MF1 achieving a temperature rise from 28°C to 56.5°C within 600 seconds. The specific absorption rate has reached 330 W/g, while the intrinsic loss power of 6.17 $nH \cdot m^2 \cdot kg^{-1}$ has significantly exceeded clinically approved ferrofluids (0.15–3.1 $nH \cdot m^2 \cdot kg^{-1}$) and has been comparable to recently reported values.

Keywords: Colloidal stability, Graphene oxide, Magnetic inductive heating, Magnetic nanoparticles

1 Introduction

Spinel ferrite magnetic nanoparticles (MNPs) are one of the multifunctional oxides with the general formula MFe_2O_4 (M^{2+}: Mn, Ni, CO, Zn, CO) utilized in diverse technological and biomedical domains due to their tunable magnetic properties, improved chemical stability, biocompatibility, and facile synthesis methods[1-3]. Despite their superior magnetic properties, MNPs are highly prone to agglomeration and lose their superparamagnetic regime (1-20 nm)[4]. These superparamagnetic spinel ferrites exhibit a single-domain nature and are highly attractive for applications in magnetic resonance imaging (MRI), targeted drug delivery, magnetic hyperthermia, supercapacitors, and environmental remediation[5]. Amongst the spinel ferrites, manganese ferrite ($MnFe_2O_4$) has emerged as an excellent choice for theragnostic applications due to the large number of unpaired spins, tunable magnetic anisotropy, and high saturation magnetization[6]. However, in pristine $MnFe_2O_4$ MNPs, the inherent high magnetic moment hampers its colloidal stability leading to rapid nanoparticle agglomeration in aqueous media. The hydrophobic surface properties and high agglomeration rate limits the practical implementation of $MnFe_2O_4$ in hyperthermia applications[7]. Surface modification strategies are highly valuable to ensure colloidal stability in the aqueous medium. The presence of hydrophilic functional groups (-COOH, NH_2, -OH) at the surface enhances aqueous dispersibility, and also provide reactive anchor sites for $MnFe_2O_4$ core MNPs. In this direction, the utilization of oxygen enriched graphene oxide (GO) for surface modification of $MnFe_2O_4$ MNPs provides an effective solution. GO improves the hydrophilicity and colloidal stability through electrostatic repulsion

*Corresponding author (E-mail: rojaleena@gmail.com)

imparted by negatively charged functional groups (-COOH, NH_2, -OH). Graphene oxide can be modified through controlled oxidation processes via the improved Hummers method, or Tour's method employing H_2SO_4/H_3PO_4 mixtures, yielding graphene with a superior degree of oxidation[8-9].

$MnFe_2O_4$ MNPs have been extensively investigated for biomedical applications such as hyperthermia and MRI[10]. Recent studies have demonstrated that chitosan-functionalized $MnFe_2O_4$ nanoparticles exhibit size-dependent specific adsorption rate (SAR) and dual-mode MRI contrast effect. The surface charge of $MnFe_2O_4$ exceeding +30 mV ensures colloidal stability for intravenous administration. Effective surface consisting of GO- $MnFe_2O_4$ magnetic nanocomposite, synthesized via coprecipitation techniques, has been successfully employed for the efficient removal of toxic heavy metal ions (Pb^{2+}, As^{3+}, As^{5+}) from contaminated water[11]. The $MnFe_2O_4$/reduced graphene oxide (rGO) nanocomposites have yielded materials with outstanding electrochemical performance for supercapacitor applications, retaining 90.22% of their capacitance after 6000 cycles, attributed to the synergistic interplay between the spinel structure and the conductive rGO matrix[12]. Surface modification of $MnFe_2O_4$ nanoparticles with polyethylene glycol (PEG), chitosan, or GO has been shown to enhance the material's hydrophilicity, thereby reducing systemic toxicity[13]. Recent literature reports that surface functionalization of $MnFe_2O_4$ MNPs is quite effective in improving therapeutic efficacy in breast cancer (MCF-7) and other malignant cell lines[14].

Despite their enormous application, the limited stability of GO under physiological conditions poses a significant challenge. Ineffective surface functionalization, long-term storage, instability towards light or elevated temperatures degrade their performance. Long-term aging induces progressive reduction of (-NH_2, -COOH, -OH) functional groups from GO[15]. The thermal decomposition of GO decreases from 216°C to 195°C, signifying a decline in thermal stability[16]. In addition, incomplete removal of oxidants such as $KMnO_4$ and H_2SO_4, or intercalated metal ions like Mn^{2+} during conventional GO synthesis can lead to the presence of cytotoxic impurities. Additionally, a limited degree of oxidation, particle size distribution, and the ratio of sp^2 to sp^3 carbon domains introduce significant batch-to-batch variability. These challenges limit the oxidized graphene for their hydrophilicity, reproducibility, and thermal stability, which is a prerequisite for hyperthermia application[17].

In this study, a novel synthesis method was employed to enhance the degree of oxidation of graphene oxide using an ultrasonication-assisted approach. The synthesized GO was successfully utilized as a surfactant for superparamagnetic $MnFe_2O_4$ MNPs. The $MnFe_2O_4$ provides a synergistic effect by magnetizing graphene oxide, which offers superior thermal stability, whereas oxidized graphene oxide provides hydrophilicity due to the presence of a higher density of carboxyl and hydroxyl functional groups. Enhanced surface functionalization of GO enables strong covalent and electrostatic attachment of $MnFe_2O_4$ nanoparticles to the graphitic matrix. The GO@MF1 exhibits excellent colloidal stability, with zeta potentials exceeding ± 40 mV, supporting long-term colloidal stability. Additionally, the calorimetric method was employed to investigate the hydrophilic GO@MF1 magnetic fluid at 585.6 kHz and 12 mT. GO@MF1 exhibits an elevated specific absorption rate (SAR) and intrinsic loss power (ILP), making it suitable for magnetic inductive heating in hyperthermia therapy.

2 Materials and Methods

2.1 Material

Graphite flakes (99.8%, natural graphite with 325 mesh), Manganese chloride ($MnCl_2$; 99%), and anhydrous ferric chloride ($FeCl_3$; 99 %) obtained from Alfa Aesar, Sodium Nitrate ($NaNO_3$; > 98%), hydrogen peroxide (H_2O_2; 30% w/v), Orthophosphoric acid (H_3PO_4; > 80-90 %), Sulphuric acid (H_2SO_4; > 97%), Sodium hydroxide (NaOH; > 98%) pallets, and potassium permanganate (KMnO4; > 98%) were purchased from Fisher scientific and directly used without any purification.

2.2 Synthesis of graphene oxide (GO)

2.2.1 Hummers' method

In Hummers' method, 69 mL of concentrated H_2SO_4 was added to a mixture of graphite flakes (3.0 g, 1 equivalent) and $NaNO_3$ (1.5 g, 0.5 equivalent), and the temperature was reduced to 0 °C. The 3 equivalents of $KMnO_4$ (9.0 g) were then gradually added in portions, keeping the temperature below 20 °C. The reaction was heated to 35 °C and stirred for 30 minutes, followed by the slow addition of water (138 mL), which caused a sharp exothermic reaction, raising the temperature to 98 °C. To maintain this temperature for 15 minutes, external

heating was applied, and afterward, the mixture was cooled in a water bath for 10 minutes. After cooling, more water (420 mL) and 30% H_2O_2 (3 mL) were added, triggering another exothermic response. The resulting graphene oxide (GO) was centrifuged at 9000 rpm for 20 minutes and washed repeatedly with water until the supernatant reached a neutral pH[18]. The obtained material was dried at 60 °C for 12 hours and ground into a fine powder using a mortar and pestle, yielding purified graphene oxide.

2.2.2 Improved method

In the Improved method, a 9:1 mixture of concentrated H_2SO_4 and H_3PO_4 (360 mL of sulfuric acid and 40 mL of phosphoric acid) was added to a mixture of graphite flakes (3.0 g) and $KMnO_4$ (18.0 g). This caused a slight exothermic reaction, raising the temperature to 35-40 °C. The mixture was then heated to 50 °C and stirred continuously for 12 hours. After cooling to room temperature, the reaction mixture was poured over 400 mL of ice, and 3 mL of 30% H_2O_2 was added. The resulting graphene oxide (GO) was separated by centrifugation at 9000 rpm for 20 minutes, repeatedly washed with water until the supernatant reached a neutral pH, and redispersed. The solid material was then dried at 60 °C for 12 hours and ground into a fine powder using a mortar and pestle, yielding purified graphene oxide[19].

2.2.3 Sonicated assisted improved method

For the sonication-assisted synthesis of graphene oxide, 3 g of graphite flakes were added to a 9:1 mixture of concentrated H_2SO_4 and H_3PO_4 (360 mL and 40 mL, respectively), followed by the gradual addition of $KMnO_4$ (18.0 g) in six equal portions at 3-minute intervals. This slow addition of $KMnO_4$ is crucial to prevent the formation of explosive byproducts, as rapidly combining concentrated $KMnO_4$ with acid can lead to highly exothermic reactions. The mixture was stirred at 400 rpm and subjected to probe sonication at 120 kHz, with the temperature maintained at 50 °C for 12 hours. After the reaction, the mixture was cooled to room temperature, and 400 mL of ice water was added along with 3 mL of 30% H_2O_2, with continued sonication. The addition of water caused a significant exothermic reaction, raising the temperature to 95 °C and changing the solution's color from dark brown to yellow. The resulting graphene oxide (GO) was separated by centrifugation at 9000 rpm for 20 minutes, washed several times, and redispersed in water until the supernatant reached a neutral pH. The solid material was dried at 60 °C for 12 hours, then ground into a fine powder using a mortar and pestle to produce graphene oxide (GO). For comparison, GO was also synthesized using the conventional Hummers method and the improved method. The graphene oxide products from these three methods were designated as GOH (GO by Hummers method), GOI (GO by Improved method), and GOSI (GO by Sonication-Assisted Improved method).

2.3 Graphene oxide functionalized $MnFe_2O_4$ (GO@MF1) magnetic nanoparticles (MNPs)

The graphene oxide, synthesized via a sonication-assisted modified protocol, was employed as a surfactant to facilitate the synthesis process. In current set of reaction, 20 mmol of $MnCl_2$ and 40 mmol of $FeCl_3$ were separately dissolved in 20 mL of deionized (DI) water in individual beakers. The two solutions were then combined and homogenized at 400 rpm for 10 minutes to ensure complete mixing. Concurrently, 0.3 g of oxygen-rich, hydrophilic graphene oxide was dispersed in 20 mL of DI water and ultrasonicated for 20 minutes to achieve uniform colloidal dispersion. The graphene oxide suspension was gradually introduced into the mixed metal chloride solution, followed by homogenization. Subsequently, 5 M NaOH was added rapidly until the pH of the mixture reached 12. The resulting alkaline dispersion was further homogenized at 600 rpm for 6 hours to promote uniform nucleation and growth of the magnetic nanoparticles. The reaction mixture was transferred into a Teflon-lined hydrothermal autoclave and heated at 180 °C for 12 hours. Upon cooling to room temperature, black magnetic nanoparticles, accompanied by NaCl as a by-product, were obtained. The solid product was repeatedly washed with a DI water–ethanol mixture to remove residual graphene oxide and salt impurities. Washing was continued until no precipitate formation was observed upon the addition of $AgNO_3$ solution, indicating complete removal of chloride ions. Finally, the purified graphene oxide-functionalized $MnFe_2O_4$ magnetic nanoparticles were collected in a petri dish and dried at 60 °C for 12 hours, yielding the final functional magnetic nanomaterials.

2.4 Sample characterization

X-ray diffractometer (Model - Rigaku ultima-IV) was utilized for phase confirmation. DLS Zetasizer (Malvern: Ultra model) was used to determine the

hydrodynamics size and zeta potential of graphene oxide synthesized by Hummers' method, Improved method, and Sonication-Assisted Improved method. Fourier transform infrared (FTIR) spectra was recorded by (NICOLET5700) in the range of 4000–400 cm^{-1} in transmission mode. The surface morphology, shape, and microstructure were evaluated by HRTEM (model FEI Tecnai S Twin) and Field Emission Scanning Electron Microscopy (FESEM). Energy-Dispersive Spectroscopy (EDS) (model EVO MA 10 VPSEM) have been used to analyses the surface topography of graphene oxide. The inductive heating experiments of the optimized $MnFe_2O_4$ magnetic nanoparticles (MNPs) were carried out in the liquid phase at a concentration of 2 mg mL^{-1} using a magneTherm hyperthermia system. The magnetic nanofluid was centrally positioned over an 18-turn solenoid coil with a diameter of 50 mm, enclosed in Styrofoam insulation to ensure near-isothermal experimental conditions. The external temperature of the setup was stabilized using a water-cooling circulation unit, while the real-time temperature of the nanofluid was monitored by a calibrated thermal sensor immersed directly in the suspension. Prior to each measurement, the magnetic nanofluids (MNFs) were ultrasonicated at 20 kHz to ensure uniform dispersion and to achieve maximum heating efficiency of the synthesized graphene-functionalized $MnFe_2O_4$ MNPs.

3 Results and Discussion

3.1 Phase identification, structural and morphology analysis

Successful synthesis of GOH, GOI, GOSI, and surface-functionalized $MnFe_2O_4$ MNPs (GO@MF1) has been established through phase identification by X-ray diffraction (XRD) analysis, as shown in Fig. 1. The absence of the (002) reflection peak at 2θ = 26.64°, which is characteristic of well-ordered graphite, confirms that the synthesized graphene oxide (GO) samples are devoid of graphite contamination[20], Fig. 1(a-d). The emergence of a pronounced (001) reflection in GOH, GOI, and GOSI, observed at 2θ values of 11.64°, 10.94°, and 10.78°, respectively, is indicative of the successful oxidation of the graphite lattice. This shift denotes an increase in interlayer spacing, with calculated d-spacings of 7.59 Å, 8.15 Å, and 8.21 Å for GOH, GOI, and GOSI, respectively, obtained using Bragg's law. The largest expansion in GOSI demonstrates that sonication during synthesis fosters a higher degree of oxidation, enhancing the disruption of graphitic domain order and increasing the incorporation of oxygen-containing functional groups (ketone, aldehyde, and carboxylic acids)[21]. This process improves homogeneity and mitigates thermal gradients within the reaction mixture, thereby promoting uniform oxidation and functionalization.

Figure 1(e) represents the XRD analysis of oxygen-rich graphene oxide surface-functionalized $MnFe_2O_4$ MNPs. The observed Bragg reflections at 2θ = 18°, 29.71°, 34.92°, 36.95°, 42.32°, 52.60°, 56.16°, 61.78°, 69.90°, and 72.80° are indexed to crystallographic planes (111), (220), (311), (222), (400), (422), (511), (440), (620), and (533), confirming the formation of a pure phase cubic spinel structure with space group Fd-3m (227), corroborated by JCPDS card no. 04-013-6574[22]. The broadening of diffraction peaks signifies nanocrystallinity in the $MnFe_2O_4$ composite. In addition, the average crystallite size and strain was calculated by Williamson-Hall (W-H) method as represented by the equation; a linear plot is plotted between β hkl.Cosθ on y-axis and 4Sinθ on x-axis. The average crystallite size of 14 nm and a lattice

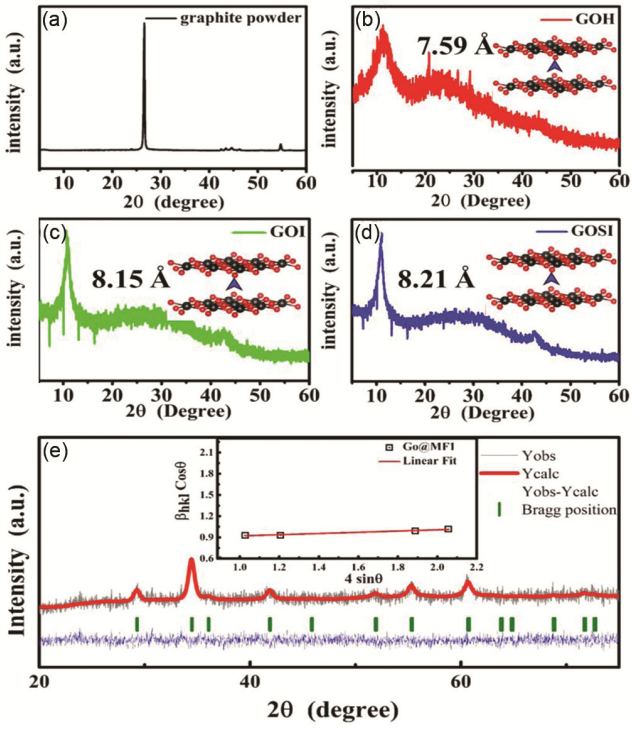


Fig. 1 — X-ray diffraction pattern of (a) Pure graphite powder, (b-d) Graphene oxide synthesized by Hummers' method (GOH), improved method (GOI), and sonicated-assisted improved (GOSI) and (e) Rietveld refined XRD structure of GOSI functionalized $MnFe_2O_4$ magnetic nanoparticles, along with an inset describing the linear fitted Williamson-Hall method.

strain of 0.00099, are determined from the linear fit. Rietveld refinement (χ^2 = 2.56) provided a refined lattice parameter 'a' of 8.485 Å and a unit cell volume of 611.04 Å³. The theoretical X-ray density of $MnFe_2O_4$ was found to be 10.02 g/cm³ based on the given formula

$$\beta_{hkl}.\mathrm{Cos}\theta = \frac{K\lambda}{D} + 4\varepsilon\,\mathrm{Sin}\theta \quad \ldots (1)$$

$$\rho x = \frac{zM}{N_A a^3} \quad \ldots (2)$$

where M is the molar mass, Z is atom count per unit cell, N_A represents the Avogadro's number, and a demonstrate the lattice constant[23].

Figure 2 illustrates the crystallographic structure of graphene-functionalized $MnFe_2O_4$ MNPs derived from Rietveld analysis. The crystal model generated by VESTA reveals that Mn^{2+} ions statistically occupy tetrahedral (A) sites while Fe^{3+} ions preferentially reside at octahedral (B) sites, consistent with crystal field stabilization energy considerations for the normal spinel structure. However, $MnFe_2O_4$ exhibits partial inverse spinel character (with approximately 20% inversion), leading to minor occupancy of Mn^{2+} at octahedral sites and Fe^{3+} at tetrahedral sites. Using standard geometric relationships and the refined lattice parameter (a = 8.485 Å), the calculated radii of tetrahedral and octahedral voids are 0.576 Å and 0.768 Å, respectively, while the positional oxygen parameter (u = 0.379) closely aligns with the ideal value for a normal spinel (u ≈ 0.375)[24]. This confirms dominant Mn^{2+} occupancy at tetrahedral sites and Fe^{3+} occupancy at octahedral sites, with slight parameter deviations arising from partial inversion. These structural insights, supported by XRD and Rietveld refinement, establish the high purity, nanoscale crystallinity, and site-specific cation distribution in the functionalized $MnFe_2O_4$ nanoparticles synthesized on graphene oxide.

Fourier-transform infrared spectroscopy (FTIR) has been used to investigate the surface functionalization of $MnFe_2O_4$ and identify characteristic functional groups present on the surface of graphene oxide (GO) nanosheets over a spectral range of 4000 cm^{-1} to 400 cm^{-1} (Fig. 3(a)). A broad and intense peak seen between 3000 cm^{-1} - 3600 cm^{-1} is due to the O–H stretching vibrations of hydroxyl groups, which shows the presence of both inter- and intramolecular hydrogen bonded adsorbed water molecules[25]. Another vibration mode at 1430 cm^{-1} indicates O-H bending vibrations. A doublet band at 2976 cm^{-1} and 2896 cm^{-1} was attributed to C-H stretching in alkanes. The IR band around 1702 cm^{-1} was associated with C=O stretching vibrations of carbonyl groups, while a band near 1620 cm^{-1} corresponded to C=C skeletal vibrations of unoxidized graphitic domains within the graphene structure. Finally, a band located between 1050 cm^{-1} and 1100 cm^{-1} was attributed to alkoxy (C-O) and epoxy (C-O-C) stretching vibrations from carboxyl groups[26-27]. The fingerprint region clearly

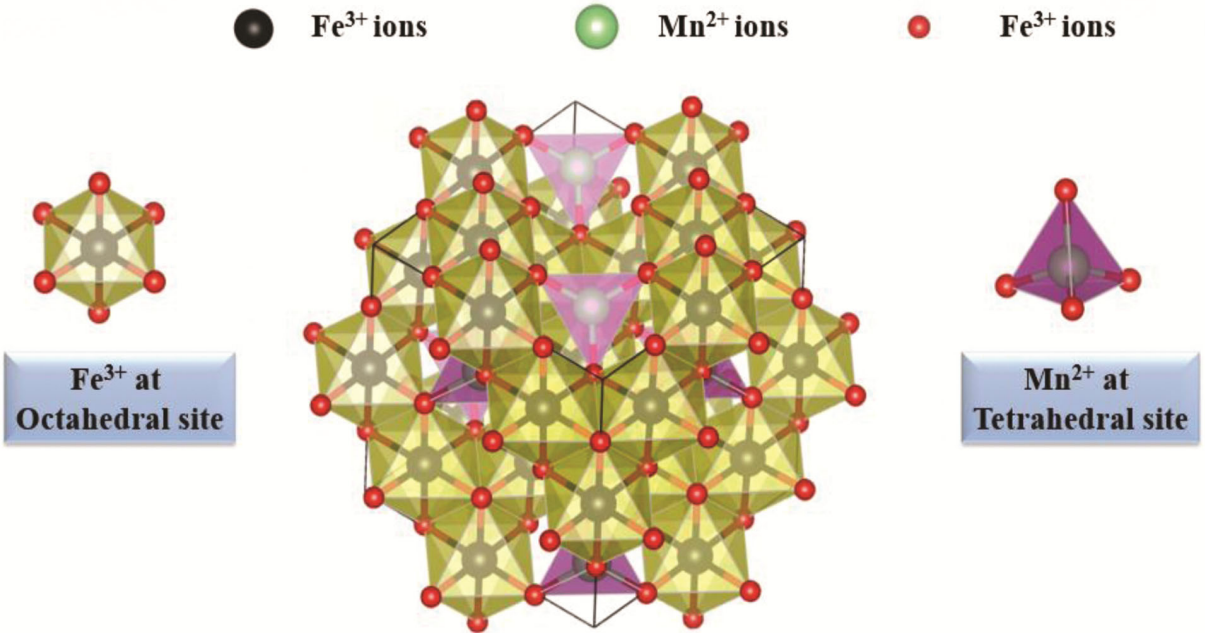


Fig. 2 — The crystallographic structure of Graphene functionalized MnFe2O4 MNPs generated from Rietveld refinement.

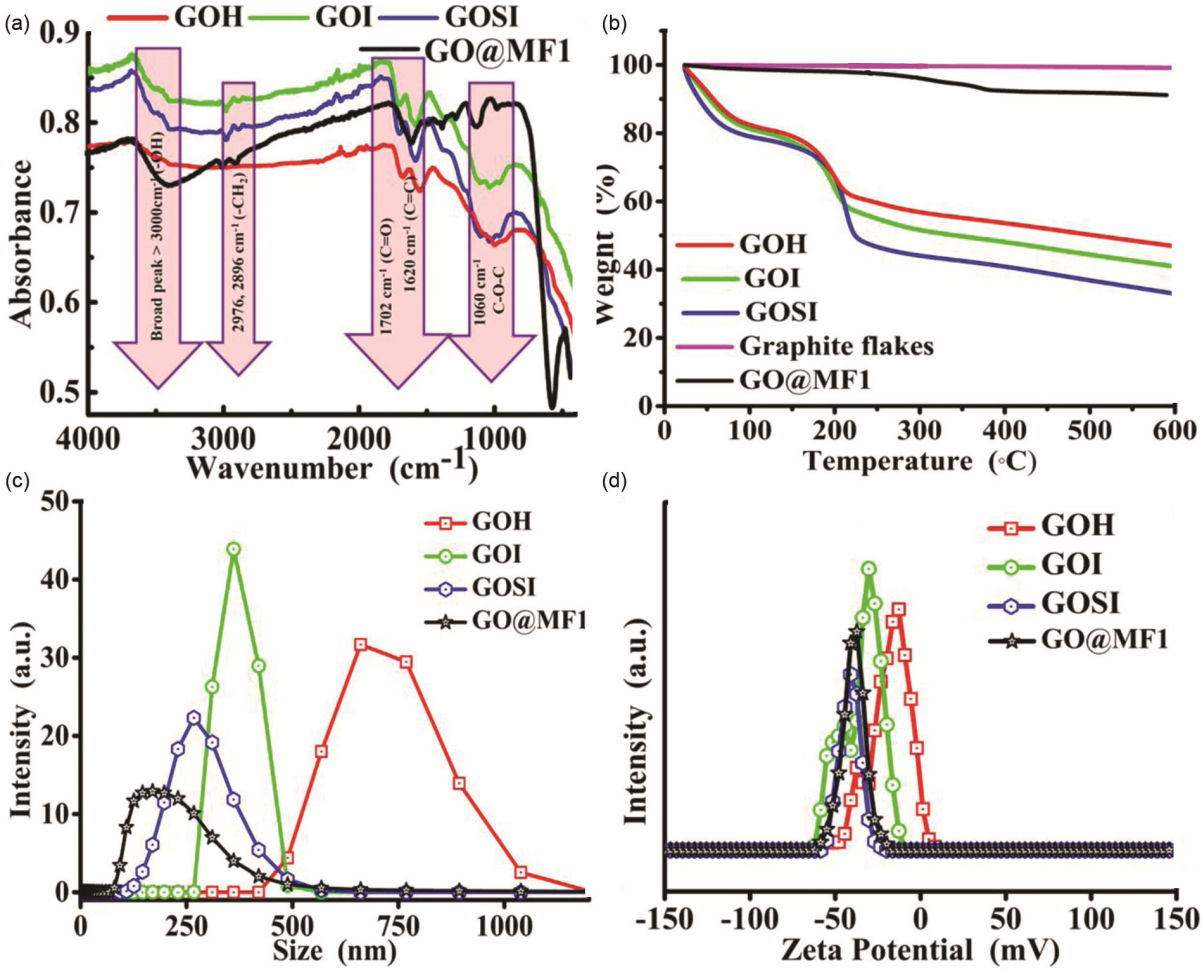


Fig. 3 — (a) Fourier transform infrared spectroscopy – ATR spectra, (b) Thermogravimetric analysis (TGA) and (c-d) Size distribution curve and zeta potential distribution determined by dynamic light scattering (DLS) of GOH, GOI, GOSI, and GO@MF1 magnetic nanoparticles.

demonstrates the Metal – Oxygen stretching frequency in the range of 400 cm^{-1} to 600 cm^{-1}. The peak observed at 567 cm^{-1} corresponds to Fe^{3+}- O^{2-} stretching frequency at octahedral site and peak at 415 cm^{-1} corresponds to Mn^{2+}- O^{2-} symmetric stretching frequency at tetrahedral site[28]. The FTIR spectra showed similar functional groups in the GOH, GOI, GOSI nanosheets, and surface functionalized $MnFe_2O_4$ MNPs.

The hydrodynamic particle size distribution of colloidal graphene oxides (GOH, GOI, GOSI), and surface functionalized $MnFe_2O_4$ (GO@MF1) MNPs has been measured using dynamic light scattering (DLS), while zeta potential (ζ) measurements were used to assess surface charge and sample homogeneity as shown in Fig. 3(c-d). For the measurements, 1 mg/mL sample was prepared in a 1:1 ethanol-water solution to enhance dispersity. The average hydrodynamic diameters of GOH, GOI, GOSI, and GO@MF1 were found to be 660 nm, 361 nm, 267 nm, and 169 nm respectively. Sonication-assisted synthesis yielded smaller hydrodynamic sizes, as prolonged sonication breaks down graphene sheets into smaller fragments. GOH exhibited the largest average hydrodynamic size, likely due to the reduced degree of oxidation during the Hummers method. Various studies suggest that the average size of GO nanosheets is influenced by the choice of oxidizing agents[29]. In addition, the GO@MF1 consist of broader hydrodynamic size distribution, which reflect the nanosized $MnFe_2O_4$ were successfully surface functionalized over oxygenated graphene oxide. The variation in hydrodynamic size totally depends over the core size and amount of hydration layer covered[28].

The effect of functionalization degree and functional group characteristics in GO was assessed

through zeta potential analysis. Typically, zeta potential values below −30 mV or above +30 mV indicate stable dispersions due to stronger inter-particle electrostatic repulsions, stemming from the ionization of functional groups in aqueous media[30]. Both the sign and magnitude of the effective surface charge help minimize particle aggregation. The average zeta potentials (ζ) of GOH, GOI, and GOSI dispersed in a 1:1 water-ethanol solution were approximately -12 mV, -31 mV, and -40 mV, respectively. The higher (more negative) zeta potential of GOSI suggests greater surface charge due to the deprotonation or ionization of carboxylic groups to carboxylate anions that leads to lower aggregation of GO sheets. In contrast, the lower zeta potential of GOH reflects higher GO sheet aggregation and a lower degree of oxidation. Therefore, GOSI is the optimum choice for using these nanosheets as a surfactant to provide colloidal stability to the magnetic $MnFe_2O_4$ MNPS. After surface functionalization, GO@MF1 exhibits the superior electrostatic repulsion evident by the ζ of -38 mV. The enhanced negative electrostatic charge provided the enhanced colloidal stability. It enables the utilization of GO@MF1 in magnetic hyperthermia applications.

The thermal stability and decomposition behavior of graphite flakes, graphene oxide synthesized via different oxidation protocols (GOH, GOI, and GOSI), and graphene oxide-functionalized $MnFe_2O_4$ magnetic nanoparticles (GO@MF1) were systematically evaluated by thermogravimetric analysis (TGA) under an N_2 atmosphere, as illustrated in Fig. 3(b). The weight (%) versus temperature profile illustrates the thermal stability, degree of oxidation, and chemisorbed surface functionalization of the synthesized $MnFe_2O_4$ MNPs in temperature ranges up to 600 °C. Superior thermal stability of graphite flakes results in minimal weight loss up to 600 °C, reflecting the inherent thermodynamic stability of the graphite structure[31]. However, the TGA profiles of GOH, GOI, and GOSI demonstrate a multistage thermal degradation primarily at 100 and 250 °C. The first stage thermal degradation of all three graphene oxide (GOH, GOI, and GOSI) samples observed at 25-100 °C is primarily attributed to the evaporation of physisorbed water molecules and low-molecular-weight volatile organic impurities adsorbed on the hydrophilic graphene oxide surface. The second stage degradation revels a more substantial and rapid weight loss (approximately 30–40%) observed at 150-250 °C, showing the thermal degradation of oxygen functional groups (-COOH, NH_2, -OH)[32]. The relative gradual weight loss observed beyond 250 °C is attributed to the slow decomposition of more thermally stable phenolic and ether functional groups attached over the graphene matrix. Notably, among the three graphene oxide variants, GOSI exhibits the steepest and most pronounced weight loss due to decarboxylation of numerous functional groups around 200-250 °C, thus indicating the highest degree of oxidation achieved through the sonication-assisted improved method[33]. The thermal stability results are well corroborated with XRD expanded interlayer spacing (d = 8.21 Å) and superior colloidal stability reflected in the zeta potential measurements (ζ = −38 mV). The TGA profile of GO@MF1 reveals markedly enhanced thermal stability relative to the graphene oxide samples. The thermal stability of GO@MF1 evident by modest weight loss of approximately 8–10 %, with decomposition occurring at around 400 °C[34].

The improved thermal stability of GO@MF1 is attributed to the chemisorption between the oxygen-rich functional groups on the GO surface and the surface-bound metal cations (Mn^{2+} and Fe^{3+}) of the $MnFe_2O_4$ spinel lattice. Here, the presence of thermally stable $MnFe_2O_4$ phase mitigates heat-induced degradation of the organic component. The retention of a substantial residual mass even at 600 °C in the GO@MF1 nanocomposite further confirms the predominance of the inorganic $MnFe_2O_4$ phase and validates the successful surface functionalization of the $MnFe_2O_4$ MNPs with graphene oxide.

The surface morphological characteristics of graphene oxide synthesized by sonication-assisted improved method (GOSI) and graphene oxide-functionalized $MnFe_2O_4$ (GO@MF1) magnetic nanoparticles have been systematically investigated by field emission scanning electron microscopy (FESEM), as depicted in Fig. 4(a-b). The high-magnification FESEM micrograph, Fig. 4(a), reveals the characteristic morphology of exfoliated graphene oxide nanosheets, exhibiting well-defined interlayer spacing with a distinctive wrinkled structure showing different layers. The pronounced interlayer expansion observed in the FESEM image of GOSI sample is attributed to the enhanced oxidation efficiency achieved through the novel ultrasonication-assisted improved GO synthesis. The transmission electron microscopy

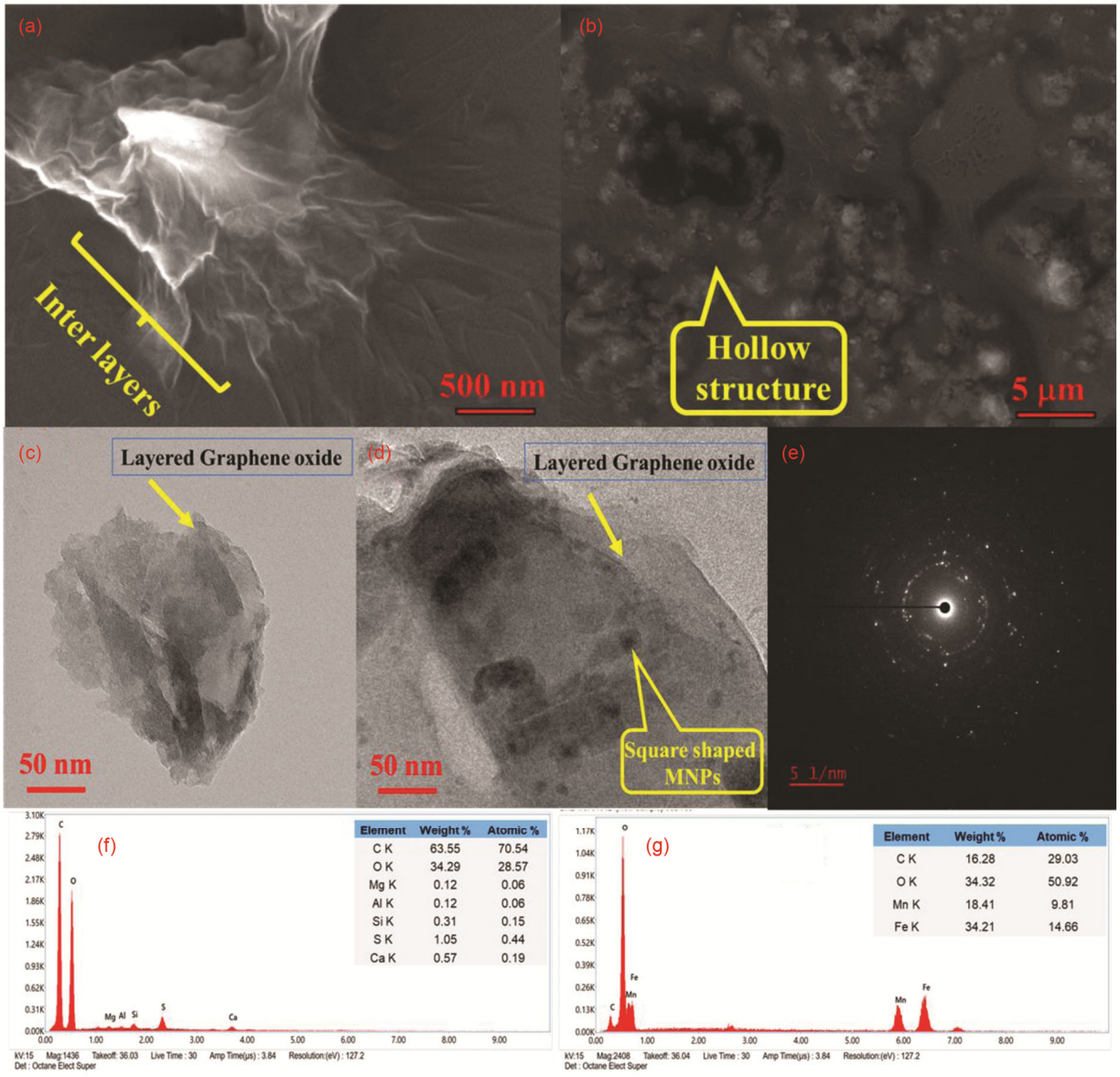


Fig. 4 — FESEM and HRTEM images of (a, c) graphene oxide, (b, d) GO-functionalized $MnFe_2O_4$ nanoparticles (GO@MF1), (e) SAED pattern of GO@MF1 showing polycrystalline structure and (f, g) EDX spectra displaying elemental compositions of GO and GO@MF1, respectively.

(TEM) image of GOSI shown in Fig. 4(c) further verifies the interlayer expansion with well-defined lamellar morphology. This ultrasonication assisted GO synthesis facilitates uniform intercalation of oxygen-containing functional groups between adjacent graphitic layers. An expanded interlayer structure provides sufficient space for accommodation of the magnetic nanoparticles, and is also consistent with the XRD-derived d-spacing of 8.21 Å in GOSI. The broader perspective presented in Fig. 4(b) demonstrates the successful encapsulation of $MnFe_2O_4$ nanoparticles having cubic morphology, within the interlayers of the graphene oxide matrix. Some hollow structures are also visible that may have arisen due to the preferential surface nucleation facilitated by the oxygen-rich functional sites on the GO nanosheets[35]. This interfacial integration between the magnetic nanoparticles and the graphene oxide nanosheets confirms the significant role of sonication-assisted methodology in producing highly oxidized GO with widened interlayer spacing. The TEM image in Fig. 4(d) demonstrates the successful in-situ

formation and encapsulation of cubic-shaped $MnFe_2O_4$ nanoparticles within the interlayer galleries of the graphene oxide matrix (GO@MF1). The corresponding selected area electron diffraction (SAED) pattern shown in Fig. 4(e) exhibits distinct polycrystalline diffraction rings corresponding to the characteristic lattice planes of cubic spinel $MnFe_2O_4$, which are in excellent agreement with the XRD planes indexed to the space group Fd-3m (227)[36]. The well-defined diffraction spots and ring patterns confirm the high crystallinity and phase purity of the encapsulated $MnFe_2O_4$ nanoparticles, with no evidence of secondary phase formation or structural distortion.

The elemental composition and stoichiometric distribution within the synthesized GO@MF1 were systematically characterized by energy-dispersive X-ray spectroscopy (EDS), as shown in Fig. 4(f-g). The quantitative elemental analysis of GOSI in Fig. 4(f) reveals the predominance of carbon (C) and oxygen (O) with trace amounts of Mg, Al, Si, S and Ca attributed to residual impurities originating from the graphite precursor or introduced during the oxidative synthesis process. In contrast, the EDS spectrum of GO@MF1 in Fig. 4(g) depicts the presence of Mn and Fe as prominent elements, along with C and O. An approximate Mn:Fe atomic ratio of 1:2 substantiates the successful in-situ nucleation, growth, and encapsulation of cubic spinel $MnFe_2O_4$ nanoparticles within the graphene oxide matrix, as evidenced by the FESEM and TEM micrographs. The high amount of oxygen in EDS is due to the presence of -COOH, -NH_2, -OH functional groups on the GOSI surface as well as the lattice oxygen in the $MnFe_2O_4$ spinel structure, thereby confirming effective interfacial bonding between the GO@MF1. The presence of carbon in GO@MF1 verifies the retention of the graphene oxide framework throughout the hydrothermal synthesis, ensuring structural integrity and the availability of functional sites for subsequent hyperthermia applications.

3.2 Magnetic properties analysis

The magnetic properties of GO@MF1 were systematically investigated for the field-dependent magnetization behavior and suitability for hyperthermia applications. Vibrating sample magnetometry (VSM) measurements were performed at room temperature, and the M–H curves were fitted via the approach to saturation (ATS) method, as shown in Fig. 5(a). The characteristic magnetic parameters such as coercivity (H_c), saturation magnetization (M_s), remanent magnetization (M_r), and the ratio of remanence to saturation magnetization (M_r/M_s), were extracted from the M-H hysteresis curve. As detailed in the inset of Fig. 5(a), the synthesized GO@MF1 MNPs exhibited a notably minimized coercivity of 17 Oe, significantly lower than the typical superparamagnetic threshold (< 50 Oe), indicating negligible magnetic anisotropy barriers resulting in facile magnetization reversal[37].

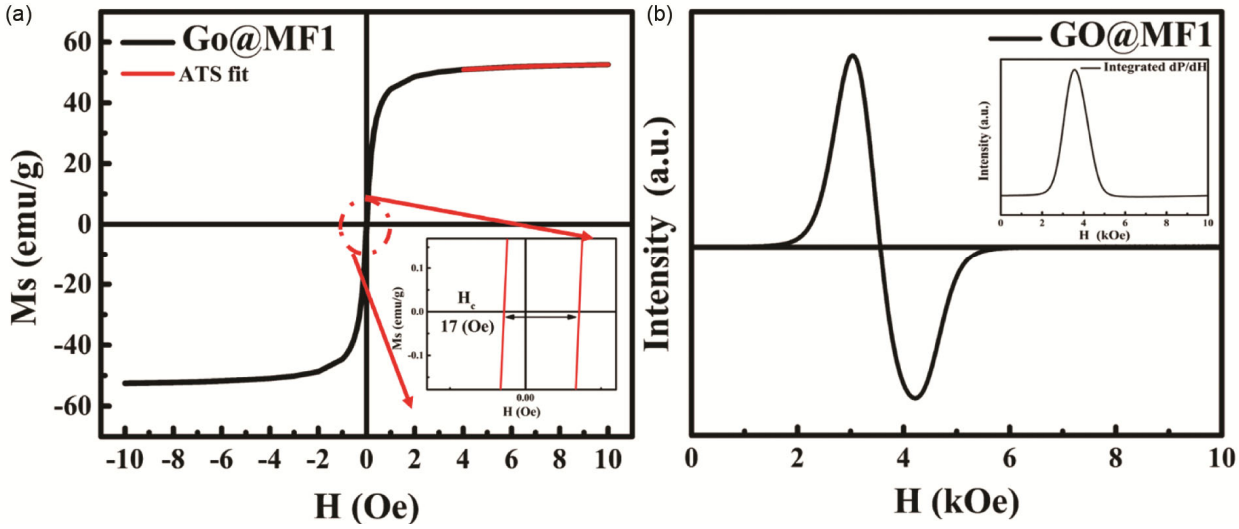


Fig. 5 — (a) Static magnetic characterization of graphene oxide functionalized $MnFe_2O_4$ magnetic nanoparticles (Go@MF1) illustrated by the room-temperature M–H hysteresis loop; the inset provides a magnified view of the low-field region, highlighting the coercive field and (b) Dynamic magnetic response measured by electron paramagnetic resonance (EPR) spectroscopy; the inset displays the corresponding integrated EPR absorption spectrum of GO@MF1.

The curve demonstrates a sharp increase in magnetization followed by rapid saturation attained within an applied field of approximately 2 kOe, confirming that GO@MF1 particles are predominantly single-domain and exhibit ideal superparamagnetic behavior at room temperature. The saturation magnetization of 56 emu/g is superior compared to previously reported graphene oxide-based magnetic nanocomposites[38], but is lower than that in the bulk $MnFe_2O_4$ (80 emu/g). This reduction in M_s is primarily attributed to pronounced surface effects, reduced crystallite size, and the diamagnetic contribution of oxygen-rich graphene oxide, which minimize core spin alignment and decrease the net magnetic moment.

From an application perspective, the low coercivity and high saturation magnetization of the oxygen-enriched GO@MF1 MNPs make them optimal candidates for magnetic hyperthermia. The reduced coercivity translates to enhanced energy dissipation under alternating magnetic fields. Furthermore, magnetocrystalline anisotropy has been quantified using the approach to saturation (ATS)[39]:

$$M(H) = \chi_{HF} + m_s\left(1 - \frac{a}{H} - \frac{b}{H^2}\right) \quad \ldots (3)$$

where, $M(H)$ denotes field-induced magnetization, M_S is the saturation magnetization, H is the externally applied magnetic field, and the constants a and b correspond to contributions from intrinsic defects and magnetocrystalline anisotropy, respectively. The effective magnetocrystalline anisotropy (K_{eff}) was found within the theoretically optimal range (0.5×10^4 - 4×10^4 J/m³). The high specific absorption rates (SAR) also reinforce the material's suitability for hyperthermia therapy applications[40].

The dynamic magnetic characteristics of GO@MF1 were investigated using electron paramagnetic resonance (EPR) spectroscopy to determine the microscopic magnetic interactions among $MnFe_2O_4$ MNPs. The EPR spectra were recorded by sweeping the external magnetic field from 0 to 10 kOe at a fixed microwave frequency of 9.5 GHz. A similar magnetic response is observed during hyperthermia measurements. Therefore, the microscopic magnetic behavior revealed by EPR provides valuable insight into the inductive heating mechanism of GO@MF1 MNPs. The interaction of magnetic spins with the applied magnetic field satisfies the Zeeman effect, which is manifested as the characteristic absorption spectrum shown in the inset of Fig. 5(b). Key spectral parameters including the resonance field (H_r), peak-to-peak linewidth (ΔHpp), g-factor, and spin–spin relaxation time, were obtained from the Lorentzian-shaped first derivative (dP/dH) curve. The resonance field and linewidth provide direct information about the electronic and magnetic environment of the lattice, as well as the degree of spin–lattice interactions[41].

In the present study, the $MnFe_2O_4$ sample exhibits a resonance field of 3597.4 Oe and a linewidth (ΔHpp) of 1153.5 Oe. The spectrum is single, broad, and symmetric, indicating the presence of a uniform spin environment primarily consisting of Mn^{2+}, Fe^{3+}, and O^{2-} ions within a well-defined spinel lattice, free from secondary impurity phases[42]. The g-value of the sample, calculated using the relation

$$g = \frac{h\nu}{\mu_B H_r} \quad \ldots (4)$$

where h is Planck's constant, ν is the microwave frequency, and H_r is the resonance field, is found to be 1.96. This value is slightly smaller than that of a free electron (2.006), suggesting that strong superexchange interactions between the cations (Mn^{2+}, Fe^{3+}) and oxygen anions dominate over dipole–dipole interactions among the nanoparticles. The high symmetry of the EPR signal, along with the obtained H_r and g-values, confirms the superparamagnetic nature of the $MnFe_2O_4$ nanoparticles, consistent with DC magnetic measurements. Furthermore, the spin–spin relaxation time (T_2) was evaluated using the relation

$$\frac{1}{\tau_1} = \frac{16\pi^2 \nu^2 \hbar}{\sqrt{3}\, g\, \Delta H_{pp}\, \mu_\beta} \quad \ldots (5)$$

where ΔH represents the full width at half maximum (FWHM) of the absorption spectrum and $\hbar$ is the reduced Planck constant. The calculated T_2 value of approximately 30 ps indicates an extremely short relaxation time, signifying rapid spin dynamics. This fast relaxation supports the predominance of Néel-type relaxation as the governing mechanism of inductive heating in $MnFe_2O_4$ MNPs. Hence, both the microscopic (EPR) and macroscopic (magnetization) analyses reveal a strong correlation between spin dynamics and the enhanced inductive heating efficiency of the synthesized nanoparticles[43].

3.3. Hyperthermia analysis

In order to determine the potential of GO for biomedical hyperthermia applications, inductive

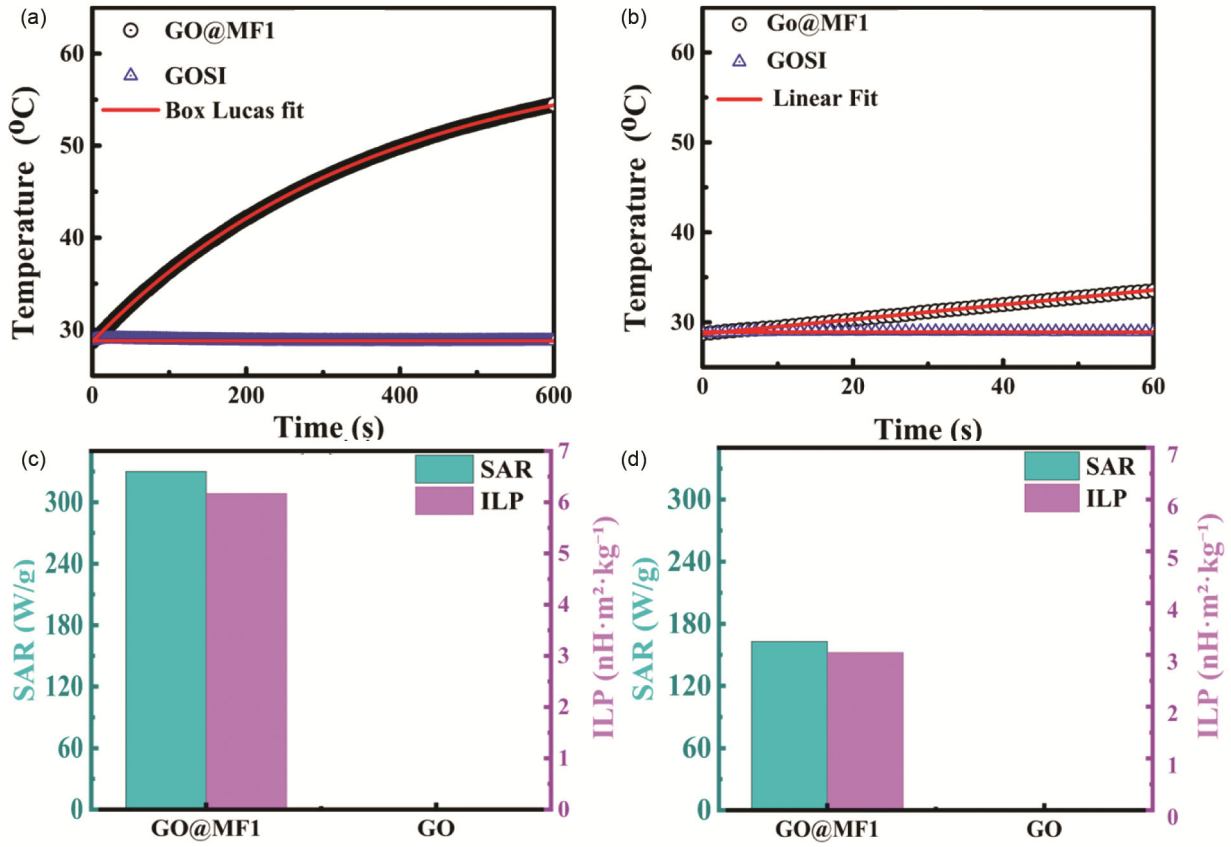


Fig. 6 — Temperature versus time inductive heating profile graph of GOSI and GO@MF1 fitted by (a) Box lucas method, (b) Linear fit method and (c-d) Corresponding SAR and ILP values.

heating experiments were performed. The heating performance was quantitatively assessed calorimetrically by exposing the nanoparticle dispersion to an alternating magnetic field (AMF) of 12 mT at a frequency of 585.6 kHz. The corresponding temperature–time profile obtained under AMF is presented in Fig. 6(a-b). The heating efficacy was characterized in terms of the specific absorption rate (SAR), representing the power absorbed per unit mass of magnetic material. SAR values were determined using the initial slope method based on the first 60 seconds of heating, following the equation[44]:

$$SAR = \frac{C \cdot (dT/dt) \cdot M_s}{M_m} \quad \ldots (6)$$

where, C is the heat capacity of the dispersion medium (4.18 J/g. Celsius), dT/dt is the initial rate of temperature increase, M_s is the mass of the dispersed solution, and M_m is the mass of the magnetic nanoparticles. Furthermore, SAR values were refined by fitting the complete heating curves using the Box–Lucas model[45], expressed as

$$\Delta T = a\left(1 - e^{(-b(t-t_o))}\right); \quad SAR = \frac{abC}{m} \quad \ldots (7)$$

where a and b are experimental parameters obtained from the fit and used in the SAR calculation. A comparative assessment of SAR values obtained from the initial slope and Box-Lucas methods is provided in Fig. 6(c-d). No measurable temperature elevation was recorded for pure GO under identical AMF conditions, confirming that GO alone does not contribute to inductive heating. This observation validates that the applied magnetic field and frequency do not intrinsically produce heating effects, and that the temperature rise originates exclusively from $MnFe_2O_4$ MNPs through magnetic hyperthermia.

In response to the applied AMF, the GO@MF1 MNPs exhibited a pronounced temperature elevation from 28 °C to 56.5 °C within 600 s, demonstrating their efficient magnetic-to-thermal energy conversion. To ensure biocompatibility and therapeutic safety, the AMF parameters were carefully maintained within the established Hergt's biosafety criterion (H_{max} x f = 5.5 x 10^9 $A \cdot m^{-1} \cdot s^{-1}$). The SAR values calculated using the

Table 1 — Comparative Table of recent literature of $MnFe_2O_4$ MNPs and the reported oxidized graphene oxide functionalized $MnFe_2O_4$ MNPs.

Material	Magnetic field (kA/m)	Frequency kHz	Concentration (mg/ml)	SAR (W/g)	ILP (nHm^2kg^{-1})	References
$MnFe_2O_4$	15.9	110	5	413	4.33	[7]
MFe_2O_4 (M; Co, Mn, Ni)	15 - 50	195	2	315	3.0	[44]
$M_xFe_{3-x}O_4$ (M = Fe, Mg, Zn)	90.7	188.8	5	87.8	0.055	[46]
$MnFe_2O_4$	4	280	0.4	217.6	-	[47]
$MnFe_2O_4$	25.7	178	5	175	1.49	[48]
GO@MF1	9.5	586.4	2	330	6.1714	This study

initial slope method for GO-functionalized $MnFe_2O_4$ and pure GO were 163.31 $W \cdot g^{-1}$ and 0.682 $W \cdot g^{-1}$, respectively, while corresponding SAR values derived from the Box–Lucas model were 330 $W \cdot g^{-1}$ and 0.6766 $W \cdot g^{-1}$. The higher specific absorption rate (SAR) obtained through the Box–Lucas model is due to its thorough consideration of the entire temperature versus time curve. In contrast to the initial slope approach, which only examines the first 60 seconds of temperature rise under nearly adiabatic conditions, the Box–Lucas fitting takes into account both continuous heating and heat dissipation to the surroundings. This reflects the conditions typical of a non-ideal, non-adiabatic system. As a result, the Box–Lucas method provides a more realistic estimation of the intrinsic heating efficiency of nanoparticles under practical experimental conditions.

The enhanced heating efficiency can be ascribed to the hydrophilic superparamagnetic behavior and uniform cubic morphology of the synthesized $MnFe_2O_4$ nanoparticles, which collectively facilitate an efficient magnetic response under AMF exposure. Furthermore, graphene oxide (GO) functionalization imparts excellent colloidal stability and effectively inhibits particle agglomeration, enabling Néel relaxation to dominate over Brownian relaxation[46]. This dynamic enhances magnetic moment oscillations and promotes superior energy dissipation during magnetic stimulation. Additionally, the intrinsic loss power (ILP) was determined to normalize the SAR values concerning experimental parameters, such as applied magnetic field amplitude and frequency, thereby allowing a more accurate comparison of heating efficiency across different studies. The ILP was calculated using the relation:

$$ILP = \frac{SAR}{H^2 f} \quad \ldots (8)$$

Where H denotes the applied magnetic field strength and f the frequency of the AMF. The calculated ILP values for GO@MF1 and GO were 6.1714 $nH \cdot m^2 \cdot kg^{-1}$ and 0.12653 $nH \cdot m^2 \cdot kg^{-1}$, respectively. The ILP of GO@MF1 significantly exceeds that of clinically approved ferrofluids, which typically range between 0.15 – 3.1 $nH \cdot m^2 \cdot kg^{-1}$, indicating substantially improved magnetic energy conversion capability. This enhanced ILP value corroborates the superior hyperthermic efficiency of GO-functionalized $MnFe_2O_4$ nanoparticles under the applied AMF, as summarized in the comparative Table 1.

4 Conclusion

This study demonstrates strategically synthesized GO functionalized manganese ferrite (GO@MF1) nanoparticles as highly efficient agents for magnetic hyperthermia applications. Oxygen-rich graphene oxide (GOSI) was synthesized using a novel sonication-assisted improved method, with interlayer spacing of 8.21 Å suitable for $MnFe_2O_4$ nanoparticle integration. GO@MF1 nanocomposite exhibits a zeta potential of −38 mV indicating colloidal stability. Electron microscopy (FESEM & TEM) revealed uniform cubic-shaped nanoparticles encapsulated within the layered graphene oxide framework, also validated by the stoichiometric composition given by EDX results. Magnetic characterization revealed excellent superparamagnetic behavior with a saturation magnetization of 56 emu/g and remarkably low coercivity of 17 Oe, facilitating efficient magnetic energy dissipation, optimal for hyperthermia applications. The GO@MF1 follows the Néel relaxation for inductive heating mechanism for magnetic hyperthermia therapy. The hyperthermia was performed at Hergt's biosafety criterion ($H \times f = 5 \times 10^9$ $Am^{-1}s^{-1}$). This involved applying an alternating magnetic field of 12 mT at a frequency of 585.6 kHz. The GO@MF1 nanocomposite demonstrated a rapid temperature increase from 28°C to 56.5°C within 600 seconds, successfully reaching the therapeutic hyperthermia range of 42–45°C, which is essential for

effective non-invasive cancer treatment. The specific absorption rate (SAR) has been determined as 330 W/g, while the intrinsic loss power attained 6.17 $nH \cdot m^2 \cdot kg^{-1}$. This ILP value substantially exceeds that of clinically approved ferrofluids (0.15–3.1 $nH \cdot m^2 \cdot kg^{-1}$) and surpasses previously reported manganese ferrite-based hyperthermia agents, demonstrating superior inductive heating.

Acknowledgment

The authors are thankful to Lingaya's Vidyapeeth deemed to be University for providing the resources to carry out this work.

References

1 Wu X, Ding Z, Song N, Li L & Wang W, *Ceram Int*, 42 (2016) 4246.
2 Vinosha P A, Manikandan A, Ceicilia A S J, Dinesh A, Nirmala G F, Preetha A C & Xavier B, *Ceram Int*, 47 (2021) 10512.
3 Cao Y, Abbasi M, Alijani H Q, Akbarizadeh M R, Iravani S, Barani M & Khatami M, *Ceram Int*, 48 (2022) 3448.
4 Patade S R, Andhare D D, Somvanshi S B, Jadhav S A, Khedkar M V & Jadhav K M, *Ceram Int*, 46 (2020) 25576.
5 Alam M W, Dhanda N, Almutairi H H, Al-Sowayan N, Mushtaq S & Ansari S A, *Appl Organomet Chem*, 39 (2025) e7962.
6 Almars A I, *Cancer Cell Int*, 25 (2025) 355.
7 Khan M A, Basheed G A, Singh M & Singh S P, *Colloids Surf A: Physicochem Eng Asp*, 717 (2025) 136747.]
8 Yu H, Zhang B, Bulin C, Li R & Xing R, *Sci Rep*, 6 (2016) 36143.
9 Li Z, Gadipelli S, Yang Y, He Y, Guo G, Li J & Guo Z, *Energy Stor Mater*, 17 (2017) 12.
10 Islam K, Haque M, Kumar A, Hoq A, Hyder F & Hoque S M, *Nanomaterials*, 10 (2020) 2297.
11 Jalilian M, Parvizi P & Zangeneh M R, *Water Environ Res*, 97 (2025) e70062.
12 Shih K Y & Tseng H Y, *ACS Omega*, 10 (2025) 4473.
13 Manoj G, Shalini M, Thenmozhi K, Ponnusamy K & Hari S, *Appl Surf Sci Adv*, 21 (2025) 100608.
14 Phalake S S, Somvanshi S B, Tofail S A, Thorat N D & Khot V M, *Nanoscale*, 15 (2025) 15686.
15 Yu W, Sisi L, Haiyan L & Jie L, *RSC Adv*, 10 (2020) 15328.
16 Kumar P, Silhavik M, Zafar Z A & Cervenka J, *J Phys Chem C*, 127 (2023) 10599.
17 Trikkaliotis D G, Christoforidis A K, Mitropoulos A C & Kyzas G Z, *Chem Eng*, 5 (2021) 64.
18 Yadav N & Lochab B, *Flat Chem*, 13 (2019) 40.
19 Marcano D C, Kosynkin D V, Berlin J M, Sinitskii A, Sun Z, Slesarev A & Tour J M, *ACS Nano*, 4 (2010) 4806.
20 Yu H, Zhang B, Bulin C, Li R & Xing R, *Sci Rep*, 6 (2016) 36143.
21 Romero A, Lavin-Lopez M P, Sanchez-Silva L, Valverde L & Paton-Carrero A, *Mater Chem Phys*, 203 (2018) 284.
22 Khan M A & Basheed G A, *Inorg Chem Commun*, 175 (2025) 114121.
23 Khan M A, Pal P & Basheed G A, *Colloids Surf A: Physicochem Eng Asp*, 673 (2023) 131734.
24 Kushwaha S & Nagarajan R, *J Phys Chem Solids*, 157 (2021) 110206.
25 Shahriary L & Athawale A A, *Int J Renew Energy Environ Eng*, 2 (2014) 58.
26 Wang H & Hu Y H, *Ind Eng Chem Res*, 50 (2011) 6132.
27 Alazmi A, Rasul S, Patole S P & Costa P M, *Polyhedron*, 116 (2016) 153.
28 Khan M A, Yadav S, Singh N & Basheed G A, *Colloids Surf A: Physicochem Eng Asp*, 709 (2025) 136166.
29 Al-Gaashani R, Najjar A, Zakaria Y, Mansour S & Atieh M A, *Ceram Int*, 45 (2019) 14439.
30 Khan M A, Chatterjee K, Saini P, Pal P & Basheed G A, *J Energy Storage*, 101 (2024) 113632.
31 Crumpton D M, Laitinen R A, Smieja J & Cleary D A, *J Chem Educ*, 73 (1996) 590.
32 Stankovich S, Dikin D A, Piner R D, Kohlhaas K A, Kleinhammes A, Jia Y & Ruoff R S, *Carbon*, 45 (2007) 1558.
33 Bohara R A, Thorat N D, Yadava H M & Pawar S H, *New J Chem*, 38 (2014) 2979.
34 Shete P B, Patil R M, Thorat N D, Prasad A, Ningthoujam R S, Ghosh S J & Pawar S H, *Appl Surf Sci*, 288 (2013) 149.
35 Shen K, Yan Y, Xue Y, Wu S, You J, Li L & Lew W S, *ACS Appl Nano Mater*, 6 (2023) 13330.
36 Li Z, Tian X, Wang J, Han G, Wang Y, Wu F & Qu S, *ACS Appl Nano Mater*, 8 (2025) 1727.
37 Lopez-Maldonado K L, De la Presa P, Betancourt L, Mancilla J P, Aquino J M, Hernando A & Galindo J E, *J Alloys Compd*, 637 (2015) 443.
38 Shen K, Yan Y, Xue Z, Wu S, You J, Li L & Lew W S, *ACS Appl Nano Mater*, 6 (2023) 13330.
39 Devi E C & Soibam I, *J Alloys Compd*, 772 (2019) 920.
40 Nemati Z, Alonso J, Martinez L M, Khurshid H, Garaio E, Garcia J A & Srikanth H, *J Phys Chem C*, 120 (2016) 8370.
41 Choppadandi M, Parmar K, Rao K, Rao K S, Singh K H, Kumar A & Kapusetti G, *Colloids Surf B: Biointerfaces*, 222 (2023) 113077.
42 Deepty M, Srinivas C, Kumar E R, Mohan N K, Prajapat C L, Rao T C & Sastry D L, *Ceram Int*, 45 (2019) 8037.
43 Lee J H, Jang J T, Choi J S, Moon S H, Noh S H, Kim J M & Cheon J, *Nat Nanotechnol*, 6 (2011) 418.
44 Sonia L C, Ningombam G S & Phanjoubam S, *J Alloys Compd*, 946 (2023) 169327.
45 Lanier O L, Korotych O I, Monsalve A G, Wable D, Savliwala S, Grooms N W & Dobson J, *Int J Hyperthermia*, 36 (2019) 686.
46 Demirci Dönmez C E, Manna P K, Nickel R, Akturk S & Van Lierop J, *ACS Appl Mater Interfaces*, 11 (2019) 6858.
47 Patade S R, Andhare D D, Somvanshi S B, Jadhav S A, Khedkar M V & Jadhav K M, *Ceram Int*, 46 (2020) 25576.
48 Etemadi H & Plieger P G, *ACS Omega*, 5 (2020) 18091.